CFD Modeling of Cryogenic Chilldown in a Complex Channel under Normal and Low Gravity Conditions

Justin Pesich[*], Daniel Hauser[†] and Jason Hartwig[‡]
NASA Glenn Research Center, Cleveland, OH, 44135

Mohammad Kassemi[§]
National Center for Space Exploration Research (NCSER)
NASA Glenn Research Center, Cleveland, OH 44135

Kiyoshi Kinefuchi[¶] and Yutaka Umemura[#]
Japan Aerospace Exploration Agency, Tsukuba, Ibaraki 305-8505, Japan

Takehiro Himeno[**]
University of Tokyo, Bunkyo, Tokyo 113-8656, Japan

Future NASA architectures have baselined cryogenic propulsion systems as well as cryogenic fluid management to support lunar missions and ultimately to support future missions to Mars. These missions will require chilling hardware down prior to engine restart as well as chilling lines and tanks prior to transferring and refueling these propulsion elements in orbit. In lieu of expensive tests conducted on-orbit, accurate predictive computational models of these chilldown processes can be used to reduce system and propellant mass as well as mission risk. To gain confidence in these computational models, appropriate anchoring and validation to experimental data in a relevant environment needs to be performed. Recent ground and sub-orbital flight experiments conducted by the Japan Aerospace Exploration Agency (JAXA) investigated chilldown of a complex channel resembling a turbopump bearing cavity at low flow rates. This work presents Computational Fluid Dynamics (CFD) model development of the chilldown experiment employing two-phase flow boiling models available in commercial CFD software STAR-CCM+ using Volume of Fluid (VOF) and the traditional Euler-Euler multiphase flow solvers. Comparisons of the numerical and experimental results under normal and low-gravity conditions are presented. An assessment of solid wall temperatures and phase distribution yielded important insights into multiphase solver choice, dependence on gravity environment, and challenges associated with cryogenic flow boiling prediction and validation.

---

*Thermal and Fluids Engineer, Fluid and Cryogenic Systems Branch, Member.
†Thermal and Fluids Engineer, Fluid and Cryogenic Systems Branch.
‡Research Aerospace Engineer, Fluid and Cryogenic Systems Branch, Associate Fellow.
§Chief Scientist, National Center for Space Exploration Research (NCSER).
¶Associate Senior Research Engineer, Space Technology Directorate I, Senior Member.
#Research Engineer, Research and Development Directorate, Member.
**Associate Professor, Department of Aeronautics and Astronautics, Senior Member.

Nomenclature

C_{ew} =   percentage of boiling that contributes to vapor generation
C_{wait} =   wait coefficient
C_p =   specific heat at constant pressure
d =   bubble departure diameter
f =   bubble departure frequency
F_A =   bubble area coefficient
g =   gravity
h =   heat transfer coefficient or enthalpy
k =   thermal conductivity
K =   bubble wall area fraction
$\dot{m}$ =   mass transfer rate
n'' =   nucleation site density
P =   pressure
q =   heat flux
S =   heat flux scaling factor for VOF transition boiling model
s =   quenching heat flux correction factor
t =   time
T =   temperature
T^+ =   nondimensional temperature based on distance from wall
u^* =   velocity scale based on wall shear stress
V =   velocity

Greek

α =   volume fraction
ρ =   density
φ =   heat flux scaling factor for VOF transition boiling model

Subscripts

boiling =   boiling heat flux
conv   =   convection
evap   =   evaporation
exp   =   experiment
inlet   =   at the inlet or inlet condition
initial =   initial condition
l   =   liquid phase
lat   =   latent heat
outlet =   at the outlet or outlet condition
quench =   quenching
sat   =   saturation
sim   =   simulation
sub   =   subcooling
sup   =   superheat
v   =   vapor phase
w   =   wall
0   =   reference condition

I. Introduction

Cryogenic fluid management (CFM) technology development will be critical to the maturation of future human missions beyond Low Earth Orbit. Future in-space systems that will benefit from CFM technology include nuclear thermal propulsion stages, ascent and descent stages, propellant fuel depots, and surface liquefaction plants. While cryogens offer significantly higher performance over storable propellants, there are challenging aspects when working with cryogenic liquids due to the thermophysical properties. For example, the low normal boiling point makes cryogens particularly susceptible to parasitic heat leak, resulting in thick insulation systems and potential boil-off of propellant. The low normal boiling point (NBP) and low surface tension make it difficult to transfer single phase liquid from a storage tank, making vapor ingestion downstream probable. Cryogenic fluid flow, coupled with large temperature gradients between ambient environment, transfer system, and fluid implies that there will be complex two-phase flow boiling and heat transfer. In-space engines require vapor-free propellant flow to avoid combustion instability issues during restart, and in-space depots will require vapor-free liquid flow in order to achieve very high liquid fill fractions in the customer spacecraft receiver tank. Before continuous, steady, vapor-free propellant liquid may flow, the transfer system must first be chilled down, therefore necessitating the desire to understand the underlying flow boiling and heat transfer associated with this transient process.

Chilldown is defined as the process of cooling propellant tank and transfer line hardware down to cryogenic temperatures so that liquid may flow between two points. For example, before restart of an in-space cryogenic engine [1, 2], the transfer system hardware connecting the tank with the engine must be chilled down quickly and efficiently. Likewise, the transfer system connecting an in-space storage depot tank with the customer receiver tank [3] must be chilled down using the least amount of mass [4].

The design and development of future in-space cryogenic storage and transfer systems depends on reliable, accurate models at low temperatures. All of the aforementioned systems have cryogenic propellant tanks and transfer lines that require accurate models of cryogenic flow boiling during transfer. The penalty for poor boiling models implies higher margins in launch propellant and higher safety factors on insulation and stored mass, leading both to higher launch mass and cost.

There are additional complexities that arise with modeling flight cryogenic systems relative to storable propulsion systems: (1) existing room temperature fluid-based models show discrepancies when compared to cryogenic two-phase data, which has been well documented, and (2) there is a general lack of reduced gravity cryogenic flow boiling data available with which to validate and anchor models; it is well known that flow boiling is a heavily gravity-dependent phenomena. While numerous ground tests have been performed, and while some aspects of cryogenic boiling have been investigated in a reduced gravity environment, such as liquid nitrogen (LN_2) and liquid hydrogen (LH_2) pool boiling tests on various heated surfaces via drop tower tests [5] as well as LN_2 flow boiling in a transfer line onboard parabolic flights [6], there has not been an end-to-end system level cryogenic transfer experiment in a sustained microgravity environment. The most recent attempt to obtain reduced gravity cryogenic chilldown data was by the Japanese Aerospace Exploration Agency (JAXA) who conducted chilldown tests on a complex channel resembling a turbopump bearing cavity using LN_2 in 1-g and onboard a sounding rocket [7]. Comparison of 1-g to low-g data revealed stark differences in chilldown performance. The slits of the test section formed liquid jets which easily reached the dead end of the test section in low-g, chilling the system down faster relative to 1-g due to an increase in inertia and wettability.

Computational Fluid Dynamics (CFD) models offer the potential to significantly improve predictive capability of cryogenic systems. CFD simulations can be used to analyze, optimize, or verify system performance as well as resolve multiple fluid flow and heat transfer phenomena in complex geometric systems. Recent 1-g CFD simulations of both storage [8-10] and transfer [11] of cryogens have shown reasonable agreement between model and experimental data. While there are many CFD models of storable or simulant fluids such as those flown onboard ISS, currently, there exists few (if any) CFD models of low-g cryogenic fluid behavior. This is due primarily to the lack of available direct low-g cryogenic test data.

The purpose of this paper is to present CFD simulations of the recently conducted reduced gravity cryogenic experiment, the JAXA turbopump chilldown tests from [7], and to validate the two-phase flow features and thermal response at three temperature sensor locations in both normal and low-gravity environments using commercial CFD code Siemens Simcenter STAR-CCM+ [12]. First a brief background of the turbopump chilldown experiment is presented. Next, a description is given on the CFD model, geometry, and initial and boundary conditions. CFD predictions of temperature at the experimental sensor locations and flow structures (or phase distribution) are then compared with the experimental results. Comparisons of multiphase flow solvers Volume of Fluid (VOF) and Eulerian Multiphase (EMP) Segregated Flow are also presented, including a discussion on the boiling models and challenges associated with each method.

II. Ground and Sub-orbital Flight Experiment Overview

JAXA designed an experimental test article based on the geometry of a cryogenic rocket engine turbopump bearing cavity to evaluate the chilldown process in terrestrial and low gravity environments. The motivation for conducting these experiments was to understand the impact of gravity on chilldown performance of the upgraded H-IIA LH$_2$/liquid oxygen (LO$_2$) launch vehicle. The baseline H-IIA rocket [13] relied on dumping a large amount of propellant overboard to achieve chilldown of the transfer system and turbopump and subsequent re-ignition of the engine; these flow rates were so high that in order to achieve the third desired burn, the third chilldown had to be conducted at significantly lower flow rates. However, the differences in performance between 1-g and reduced gravity chilldown grows as the flow rate decreases because of differences in the effect of the buoyancy force between the two gravitational environments. It is known that above a certain critical flow velocity that gravitational effects are overwhelmed by inertial forces and gravity level no longer affects flow boiling [6, 14]. Furthermore, at the time of this experiment, only simplified geometries like straight pipes had been tested to examine the effect of gravity on chilldown. Components such as turbopumps have more complex channels making it difficult to achieve efficient and quick chilldown. Both pump and turbine-side ball bearings have to be chilled down before rocket engine ignition, but it was still questionable whether the cooling process occurred in the turbine-side bearing in reduced gravity due to it being a dead end. Therefore, to improve overall performance and reliability of the H-IIA upgrade and to potentially reduce the amount of propellant consumption during chilldown, JAXA studied the effect of chilldown of the turbopump body in reduced gravity. Because it was desired to observe the entire chilldown process from single phase vapor, through film, transition, and nucleate boiling, at least 100 seconds of microgravity would be required. Drop towers can provide a few seconds of microgravity and parabolic flight typically provide 17-20 seconds of microgravity. The S-310-43 sounding rocket was thus employed as the testbed, because it provided ~200 seconds of test time at ~10^{-4} g.

A detailed description of the experimental design, methodology, and results is available in [7], only a brief description is presented here. A typical turbopump bearing cavity is illustrated in Fig. 1 and the experimental test section is shown in Fig. 2. Although the test article is shown horizontally in the blueprint, it was oriented vertically in the experiments so that the flow is against gravity. LN$_2$ was the test fluid used as a surrogate for LO$_2$. The test article was designed so that LN$_2$ enters the inlet and flows over a diffuser. Four slits were downstream of the diffuser and sized according to openings between the pump side ball bearings. Downstream of the slits was a room with an outlet and a dead end, where the dead end replicates the turbine-side bearings.
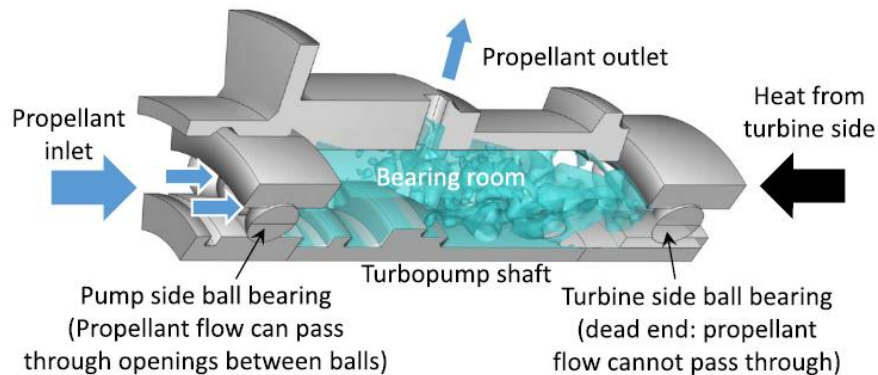

Fig. 1 Generalized turbopump section and chilldown flowpath [7]

Two identical test sections were built for different target flow rates of 1.0gram/s and 0.5gram/s named TS-A1 and TS-A2, respectively. Each test section was fabricated using polycarbonate so that the two-phase flow could be visualized through the clear material using a charge-coupled device (CCD) camera and a light emitting diode (LED) flashlight. The test sections contained three silicon diode skin-mounted temperature sensors (DT621-HR) to measure embedded solid temperatures 2 mm off the inner surface of the fluid chamber illustrated in Fig. 2 named TA1-1, TA1-2, and TA1-3. Electrostatic capacitance type void fraction sensors were installed upstream and downstream of the test sections to study two-phase flow evolution during chilldown.

The flow schematic of the experimental system is presented in Fig. 3. Void fraction, temperature, and pressure sensors were placed upstream and downstream of test sections TS-A1 and TS-A2. A pressure and temperature sensor (PKO and TKO) were placed just downstream of the main actuation valve (MAV) to determine the test section inlet

temperature and saturation condition. Video still frames were provided to visualize two-phase flow during chilldown. Test sections TS-C1 and TS-C2 were not discussed in [7].
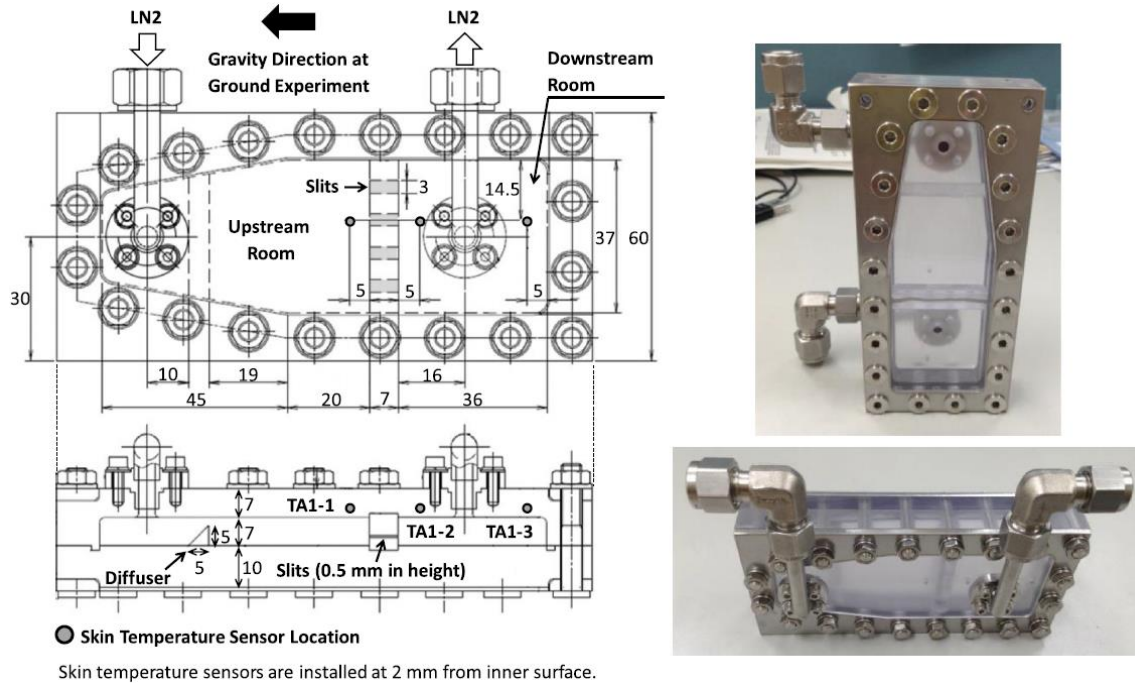

Fig. 2 Experimental test article nominal dimensions and temperature sensor locations [7]
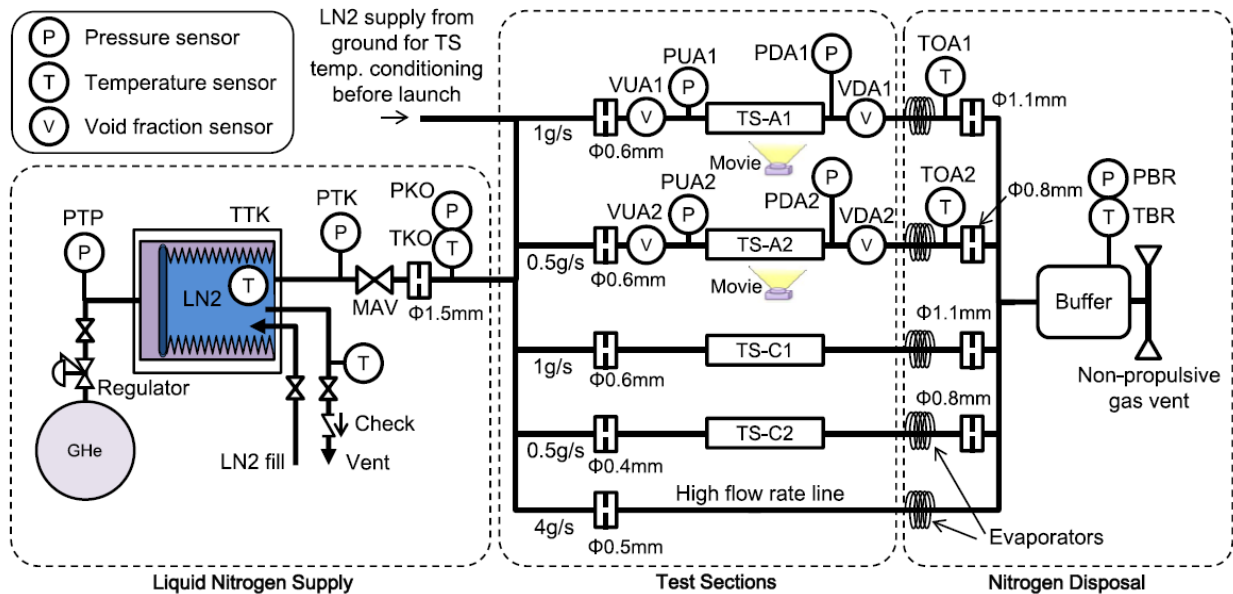

Fig. 3 Flow schematic with instrumentation layout [7]

Despite the complexity of the test and difficulty in obtaining low-g cryogenic data, results were quite clear. In 1-g, the flow direction is vertically upward, and the jets created by the slits have to overcome gravity, so there is less inertia for the flow to reach the top of the turbopump and thus chill it down; the jets from the slits spread into droplets, which barely reached the dead end. In low-g, the jet had more inertia due to the lack of gravity. So even though buoyancy was reduced in low-g, the flow did not have to overcome gravity to reach the top bearing; the jets appeared to be liquid

5

filaments and easily reached the dead end of the test sections due to the increase in jet inertia. The difference in chilldown performance between the ground and flight tests was shown to be significant, especially at the lower flow rate.

A source of uncertainty seen in both the ground and flight experiments is the quality of the mixture entering the test section. It appears that after the MAV is opened and the flow rate ramps up to the set condition of 1.0gram/s, a liquid-vapor mixture flowed through the test section for a period of time before a quality of zero is achieved. The experimental VUA1 data is presented in Fig. 4 and it is evident two-phase flow content enters the test section until the void fraction distinctly drops to zero. The time at which pure liquid injection was achieved agrees with when the inlet temperature (TKO) dropped below the saturation temperature [7]. This indicates that the fluid transfer lines must have been chilling down for ~60 seconds prior to pure liquid injection into the test section. This is an important observation that complicates inlet boundary conditions for the numerical model.
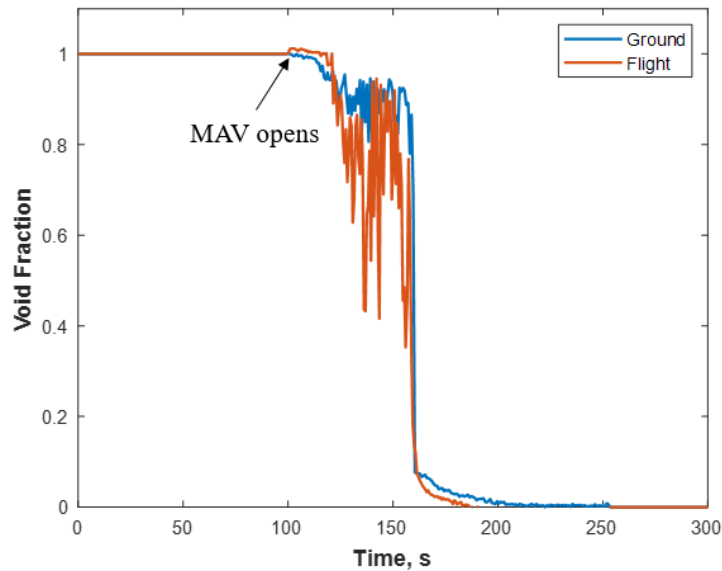

Fig. 4 Experimental void fraction data for TS-A1 [7]

III.   Computational Model

A. Multiphase Physics Models

The Volume of Fluid (VOF) Multiphase Model and Eulerian Multiphase (EMP) Segregated Flow Model in STAR-CCM+ were used in this study. Each method has its own boiling model described in the following sections, concluding with a discussion on common model parameters.

1. VOF Model Overview

The VOF model solves one set of conservation equations (continuity, momentum, energy, turbulence, etc.) for both phases. The model is typically used for systems with two or more immiscible fluid phases and uses the High-Resolution Interface Capturing (HRIC) scheme to track and sharpen the liquid-vapor interface [12]. It is possible to capture bubbles/droplets using VOF with a mesh capable of resolving these features (similar to Direct Numerical Simulation) which becomes prohibitive for large-scale problems. For the current problem, the two phases are simultaneously separated and dispersed in each other and a fine mesh for bubble/droplet resolution is impractical. Although the prediction of flow structures and phase distribution accuracy is diminished while using the VOF model, an evaluation of the boiling model was considered.

There are several advantages to using VOF over EMP. Modeling surface tension forces via the Continuum Surface Force (CSF) of Brackbill et al. [15] model is much more stable when implemented in VOF compared to EMP. Surface tension is important because these forces dominate in low-gravity environments. Additionally, VOF does not require

closure relations to define phase interactions since both phases are solved using one set of conservation equations. As a result, VOF is computationally less expensive and more stable than the EMP.

2. VOF Wall Boiling Model

The VOF model offers the Rohsenow and the transition boiling models. The Rohsenow model uses an empirical correlation to calculate the wall heat flux and is recommended in the nucleate boiling regime under terrestrial conditions. The transition boiling model aims to match the wall heat flux as a function of wall superheat through the nucleate and transition boiling regimes. For the current problem, the wall superheat is expected to cover all three boiling regimes (including film boiling), so the transition boiling model is used. Conveniently, the wall heat flux relationship can be defined separately for 1-g and low-g using experimental data. Wall superheat, or excess temperature, is defined in Eq. 1.

$$\Delta T_{sup} = T_w - T_{sat} \tag{1}$$

The wall heat flux is defined in a piecewise manner shown in Fig. 5 [12]. Experimental data for pool boiling of LN_2 along a vertical wall in 1-g and low-g were taken from [16]. This curve is used due to availability of the data, but a flow boiling curve for LN_2 would be more accurate.

The curve fit and digitized experimental data are plotted in Fig. 6 with the chosen parameter values listed in Table 1. The curve fit does not capture the film boiling regime heat flux because the convective and radiative heat fluxes, which are dominant in the film boiling regime, are not accounted for in the piecewise approximation. Convective heat flux is inherently captured by solving the flow and energy equations simultaneously. Radiation is not considered in this study, and the drawback is that the model neglects vapor generation while the wall superheat is within the film boiling regime ($\Delta T_{sup} > \sim 30K$). For the transition and nucleate regimes, the mass transfer over the area that nucleation sites cover is defined by Eq. 2 where h_{lat} is the latent heat and C_{ew} is an empirical constant related to the probability of forming boiling bubbles from nucleation sites that develop on the heated wall (default is 0.1). This serves as a limiter to how many nucleation sites turn into bubbles and all the uncertainties in bubble formation (surface roughness, contact angle, etc.) are lumped into this constant. The constant can be tuned and is dependent on problem definition; the default value was used in this study. The heat and mass transfer is applied to the computational cells next to the solid wall boundary. Note that mass transfer at the liquid-vapor interface is assumed negligible.
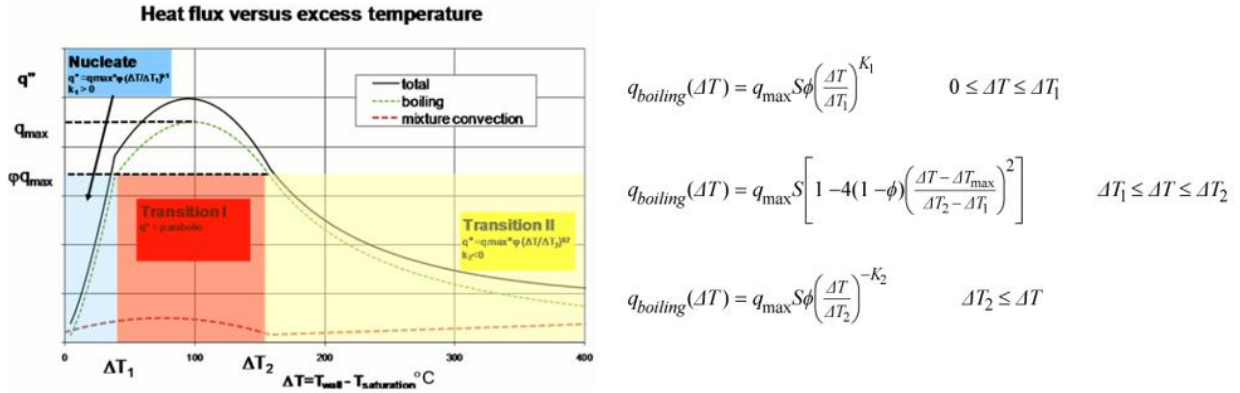

$$q_{boiling}(\Delta T) = q_{max}S\phi\left(\frac{\Delta T}{\Delta T_1}\right)^{K_1} \qquad 0 \le \Delta T \le \Delta T_1$$

$$q_{boiling}(\Delta T) = q_{max}S\left[1 - 4(1-\phi)\left(\frac{\Delta T - \Delta T_{max}}{\Delta T_2 - \Delta T_1}\right)^2\right] \qquad \Delta T_1 \le \Delta T \le \Delta T_2$$

$$q_{boiling}(\Delta T) = q_{max}S\phi\left(\frac{\Delta T}{\Delta T_2}\right)^{-K_2} \qquad \Delta T_2 \le \Delta T$$

Fig. 5 Piecewise definition of boiling curve for STAR-CCM+ VOF Transition Boiling Model [12]

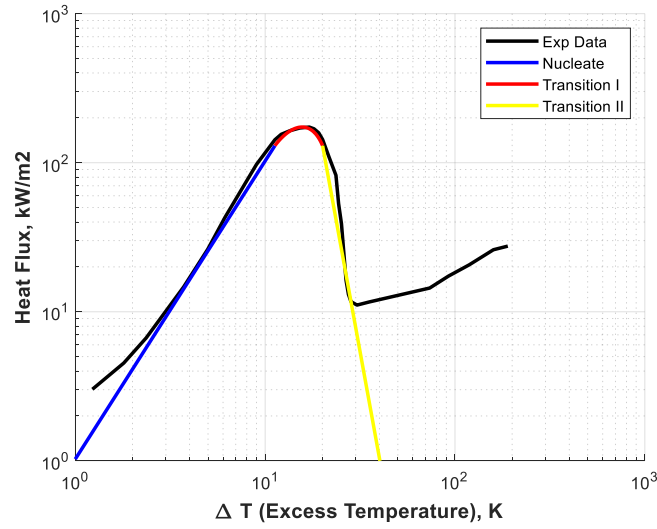**Fig. 6 Piecewise curve fit for LN2 boiling curve in 1-g [16]**

Table 1. Parameter values for piecewise boiling curve equations in 1-g

q_{max}, kW/m^2	173.44
$k1$	2.0
$k2$	7.0
$\Delta T1$, K	11.25
$\Delta T2$, K	20.07
S	1.0
φ	0.75

$$\dot{m} = \frac{C_{ew}\dot{q}''_{boiling}}{h_{lat}} \tag{2}$$

3. EMP Model Overview

   The EMP model solves a set of conservation equations for each phase. The model is typically used for two-phase flows in which one phase is dispersed in another. It is possible to model a system in which two phases are simultaneously separated and dispersed in each other using the Multiple Flow Regime Phase Interaction Model, a submodel of EMP. STAR-CCM+ defines the criterion for each flow regime and the associated flow topology shown in Table 2 [12].

Table 2. Multiple Flow Regime definitions [12]

Classification Criterion	Flow Regime	Flow Topology
$0 < \alpha_s < \alpha_{fr}$	First (dispersed) regime	Secondary phase is dispersed in primary phase.
$\alpha_{fr} < \alpha_s < \alpha_{sr}$	Interface regime	Both phases are separated.
$\alpha_{sr} < \alpha_s < 1.0$	Second (dispersed) regime	Primary phase is dispersed in secondary phase

8

Here, α_s is the volume fraction of the secondary phase, α_{fr} is the terminus of the first regime. It is the value of α_s at which the first regime transits to the interface regime. The default value is 0.3. The onset of the second regime is α_{sr} and corresponds to the value of α_s at which the interface regime transits to the second regime. The default value is 0.7. For stability reasons, the terminus of the first regime was set to 0.4 and the onset of the second regime was set to 0.6. This collapses the interface regime where the solver is less stable. For this problem, the primary and secondary phases are the liquid and vapor, respectively. The Large Scale Interface Detection model, another submodel of EMP, was used to identify groups of cells that contain a large interface and sharpens the interface by reducing the thickness to one cell. This helps to maintain a smooth interface between the separated regions of liquid and vapor.

Closure models are required to define the interactions between the liquid and vapor phases since each phase has its own set of conservation equations. The closure models used for this problem are listed in Table 3. The methods chosen are suggestions given in the STAR-CCM+ user guide based on problem definition. Interaction length scale values are left at default since this data is limited in literature. Other closure models not selected include Lift Force, Virtual Mass Force, and Turbulent Dispersion Force.

The primary advantage of the EMP model is the ability to resolve dispersed phases within a continuous phase, and EMP has a more sophisticated boiling model described in the following section. However, the complexity of the EMP modeling strategy is evident. It requires sufficient time and understanding to accurately model two-phase flows. The computational expense of EMP is substantial (more than 2X VOF), and EMP becomes unstable and produces an unphysical solution while modeling surface tension. Because of these drawbacks, EMP is only used to model the *Chilldown 1-g* case described below.

Table 3. Phase interaction closure model definitions

Closure Model	Regime	Method/Value
Drag Force	1st Regime Cd	Schiller-Naumann
	Intermediate Regime Cd	Strubelj-Tiselj
	2nd Regime Cd	Schiller-Naumann
Interaction Area Density	1st Regime	Symmetric
	2nd Regime	Symmetric
Interaction Length Scale	1st Regime	0.001
	2nd Regime	1.00E-04

4. EMP Wall Boiling Model

The EMP boiling model uses a partitioned wall heat flux approach where the heat flux is split into three components given by Eq. 3: evaporation, quenching, and convection of the mixture. The wall heat flux component definitions are given in Eqs. 4-6. The convective heat flux is determined by the local flow properties and local temperature gradient between the wall and the mixture.

The evaporative heat flux is a function of three boiling parameters: nucleation site density (n''), bubble departure frequency (f), and bubble departure diameter (d_w). Nucleation site density (Lemmert Chawla [17, 18]) and bubble departure diameter (Tolubinsky Kostanchuk [19]) are expressed as correlations that were developed based on experiments of subcooled water flowing in a vertical pipe at 45 bar and 0.57 MW/m^2 in 1-g by Bartolomei and Chanturiya [20]. Bubble departure frequency is expressed as a correlation known as the Cole model [21] that was developed by photographic study of pool boiling using water. These correlations are given in Eqs. 7-9. The evaporative mass flux is shown with the evaporative heat flux in Eq. 5 and determines the vapor generation. The heat and mass transfer is applied to the computational cells next to the solid wall boundary. Note that mass transfer at the liquid-vapor interface is assumed negligible.

The quenching heat flux represents the enhancement of heat transfer due to cool liquid replacing a departing bubble. This component is a function of the local temperature gradient between the wall and liquid, a heat transfer coefficient defined by the Del Valle Kenning model [22, 23], and a correction factor, where h_{quench} and s_{quench} are defined in Eqs. 10 and 11, respectively.

$$\dot{q}_w'' = \dot{q}_{conv}'' + \dot{q}_{evap}'' + \dot{q}_{quench}'' \tag{3}$$

$$\dot{q}''_{conv} = \frac{\rho_{mix}c_{pmix}u^*_{mix}}{T^+_{mix}}(T_w - T_l) \tag{4}$$

$$\dot{q}''_{evap} = n''f\left(\frac{\pi d_w^3}{6}\right)\rho_v h_{lat} \quad \text{with} \quad \dot{m}''_{evap} = \frac{\dot{q}''_{evap}}{h_{lat}} \tag{5}$$

$$\dot{q}''_{quench} = h_{quench}s_{quench}(T_w - T_l) \tag{6}$$

where h_{quench} is the quenching heat transfer coefficient and s_{quench} is a correction factor.

$$n'' = n_0''\left(\frac{\Delta T_{sup}}{\Delta T_{sup,0}}\right)^{A+B\left(\Delta T/\Delta T_{sup,0}\right)} \tag{7}$$

$$f = \sqrt{\frac{4g(\rho_l - \rho_v)}{3d_w\rho_l}} \tag{8}$$

$$d_w = d_0 exp\left[-\frac{\Delta T_{sub}}{\Delta T_{sub,0}}\right] \quad \text{where} \quad \Delta T_{sub} = T_{sat} - T_l \tag{9}$$

$$h_{quench} = 2K_{quench}f\sqrt{\frac{\rho_l c_{pl}k_l t_{wait}}{\pi}} \quad \text{where} \quad K_{quench} = F_A\frac{\pi d_w^2}{4}n'' \quad \text{and} \quad t_{wait} = \frac{C_{wait}}{f} \tag{10}$$

$$s_{quench} = \frac{T_w - T_{quench}}{T_w - T_l} \tag{11}$$

The nucleation site density is a strong function of wall superheat. The user can adjust the reference nucleation site density value (n''_0) and calibration constants A and B to match experimental data for a given fluid under specified conditions. $\Delta T_{sup,0}$, is the reference wall superheat and is typically set to unity. The bubble departure diameter is a strong function of liquid subcooling. $\Delta T_{sub,0}$ is the reference subcooling and the reference departure diameter (d_0) is the bubble departure diameter corresponding to the reference subcooling.

h_{quench} is a function of bubble departure frequency, local flow properties, and the bubble wall area fraction (K_{quench}) which defines the area that is affected by incoming quenching liquid. F_A is an area coefficient for scaling between the nucleation site area density and the wall area fraction the bubble-induced quenching influences and its default value is set based on the Bartolomei and Chanturiya experiment. The elapsed time between bubble departure and the nucleation of the next bubble is defined by t_{wait}, where C_{wait} is the wait coefficient and is set to 0.8. This assumes quenching occurs between the departure of one bubble and before the nucleation of the next with a period of 80% of the departure cycle.

s_{quench} is a function of local temperature gradients where T_{quench} is the temperature of the liquid replacing the bubble. The default values are used for the adjustable parameters in the correlations and are listed in Table 4. For parameters not defined in this section, reference the nomenclature. For more information regarding the EMP wall boiling model and its parameters, refer to [12].

Table 4. Adjustable EMP boiling parameter values

Parameter	Value
n''_0, /m^2	12366.45
A	1.805
B	0
$\Delta T_{sup,0}$, ΔK	1
d_0, mm	0.6
$\Delta T_{sub,0}$, ΔK	45
F_A	2
C_{wait}	0.8

It is noted here once more that the EMP boiling model was built for subcooled water flowing in a vertical pipe at a specified pressure and heat load. There is a need to develop the correlations for nucleation site density, bubble departure frequency and bubble departure diameter for cryogenic fluids in relevant environments in order to progress the maturity of flow boiling CFD models.

5. Common Model Parameters

Model parameters that are common between VOF and EMP and shown in Table 5. First order time integration is recommended by STAR-CCM+ for multiphase flow solvers.

Table 5. Common model parameters

Time step	0.001s
Transient Solver	Implicit Unsteady
Temporal Discretization	1st Order
Flow Solver	Segregated
Flow Convection Discretization	2nd Order
Volume Fraction Convection Discretization	2nd Order
Energy Discretization	2nd Order
Turbulence Model	Laminar

B. Geometry

The computational domain consists of one fluid region and two solid regions displayed in Fig. 7 with the mesh shown in Fig. 8. Half of the test article was modeled due to symmetry. Three virtual point probes (TA1-1, TA1-2, TA1-3) were placed in the locations of the embedded temperature sensors shown in Fig. 2. The outlet was extended and bent 90 degrees in the direction of the gravity vector with a convergent nozzle to provide a favorable pressure gradient and avoid numerical instabilities caused by reversed flow at the outlet. A conformal mesh was created between each of the regions to solve the conjugate heat transfer. A mesh independence study was carried out and is summarized in Table 6. Each mesh provided similar chilldown profiles at the three temperature sensor locations and almost identical average wall temperatures, so the coarse mesh was used in this study.

Table 6. Mesh comparison

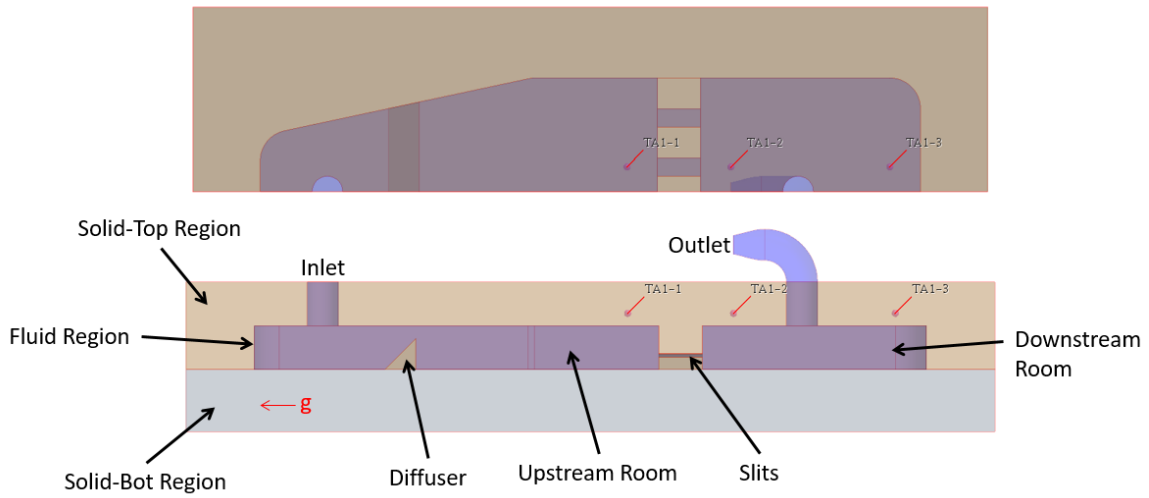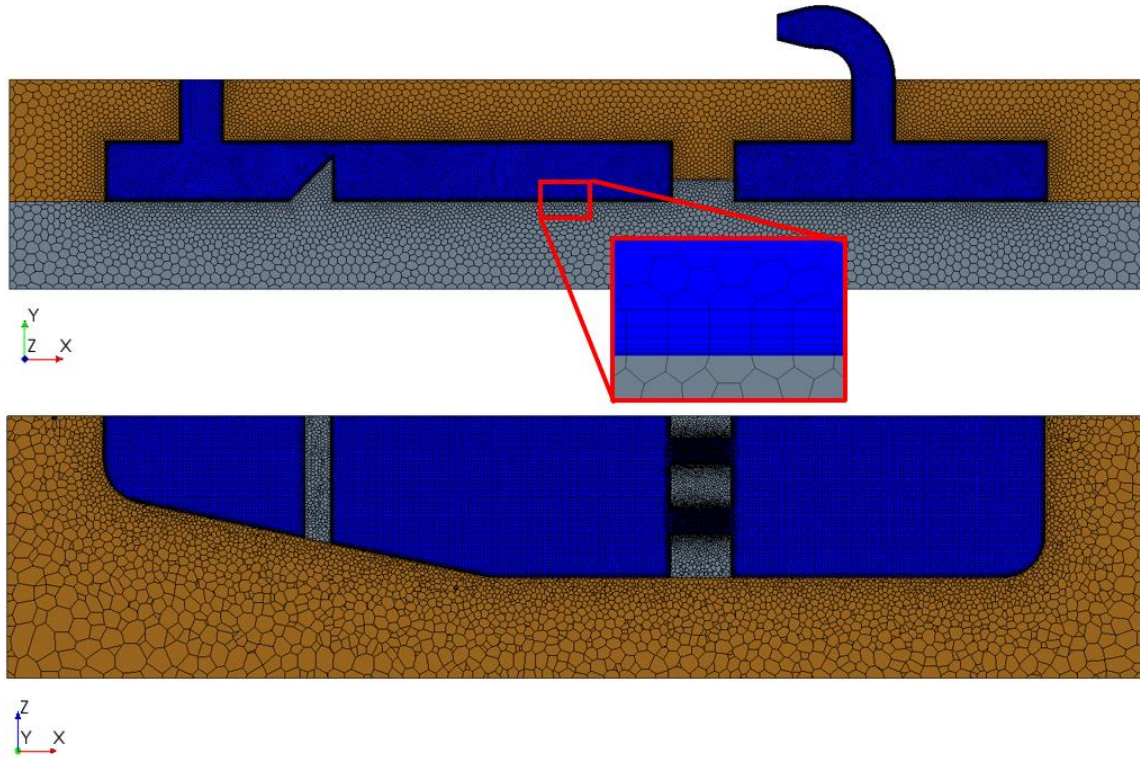|	Cell Count	Base Cell Size, mm
Coarse	1033012	0.375
Medium	1447543	0.3375
Fine	1659788	0.31875

Fig. 7 Computational model geometry

Fig. 8 Computational mesh

C. Initial Conditions and Boundary Conditions

Two cases were considered while modeling the experiment. The first case, named *Chilldown 1-g,* simulates a relatively short window of the experiment and is solved using both the VOF and EMP models. The second case, named *Liquid-Vapor Mixture Cooling + Chilldown 1-g/Low-g,* simulates a much larger window of the experiment and is solved using only the VOF model. Because the EMP model is so computationally expensive and unstable with surface tension, it was only employed in the *Chilldown 1-g* case. The motivation for each case is highlighted in Fig. 9 where the measured flow rate for the ground and flight experiments are shown. The flow rate ramps up to the set condition of 1.0gram/s and remains constant for a period of time before dramatically increasing. Referring back to Fig. 4, the

12

Mixture Cooling window models a two-phase flow inlet condition while the *Chilldown 1-g/Low-g* window corresponds with pure liquid injection.
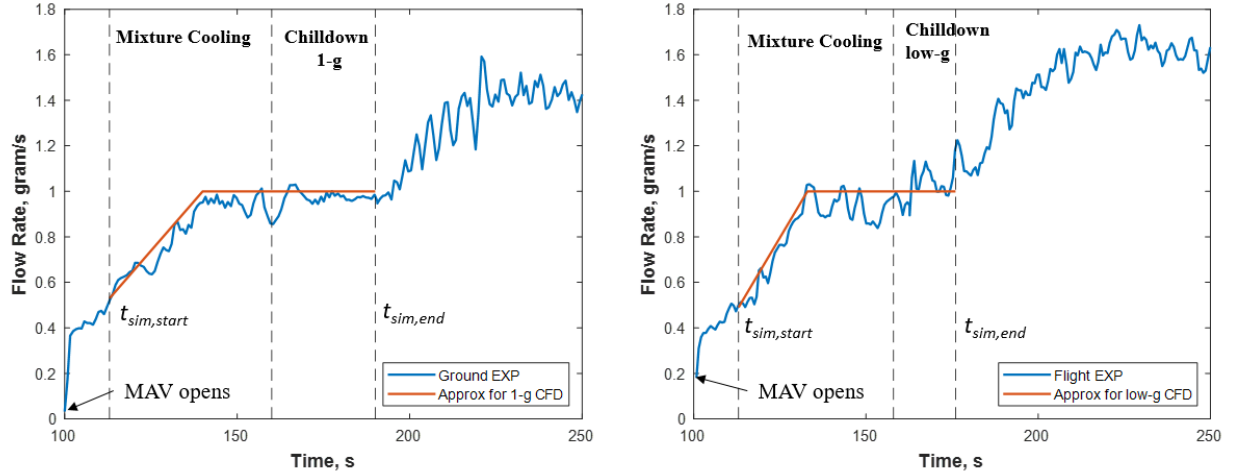
Fig. 9 Definition of simulation windows for 1-g (left) and low-g (right) [7]

1. Chilldown 1-g

The first set of simulations targeted the window of the experiment where the inlet mass flow rate was held constant for 30 seconds and the inlet void fraction was zero. This window starts 60 seconds after the MAV is opened. The initial conditions and boundary conditions for this case were extracted from the ground experimental data for the 1.0gram/s flow rate test section and are listed in Table 7. The fluid domain is initialized with 100% vapor to a uniform temperature and pressure with zero velocity. Pure liquid enters the domain at a constant mass flow rate and temperature where the liquid is ~6K subcooled at the operating pressure. The outlet face is specified as a pressure outlet and set to zero gauge pressure. No-slip boundary conditions are applied to all fluid domain walls and all solid walls are adiabatic. This case was run using both the VOF and EMP models under terrestrial conditions.

Table 7. Initial and boundary conditions, Chilldown 1-g

Variable	Chilldown 1-g
g, m/s^2	9.81
$\dot{m}_{inlet}$, gram/s	1.0
T_{inlet}, K	87
$T_{initial}$, K	173.5
T_{sat}, K	93.987
P_{outlet}, MPaA	0.5
$P_{initial}$, MPaA	0.5
$\alpha_{v,inlet}$	0
$\alpha_{v,initial}$	1
$V_{initial}<i,j,k>$, m/s	<0,0,0>
$t_{sim,start}$, s	160
$t_{sim,end}$, s	190

13

2. Liquid-Vapor Mixture Cooling + Chilldown, 1-g and Low-g

The second set of simulations targeted a larger window of the simulation where the inlet mass flow rate and inlet void fraction become heavily time-dependent. These longer time history simulations were split into two sections. The first section is designated *Mixture Cooling* where the inlet condition is predominately vapor and some small percentage of liquid. The second section is designated *Chilldown* where the inlet condition is 100% liquid and is identical to the *Chilldown* setup described in the previous section except the initial conditions are defined by the final state of the mixture cooling simulation.

The initial conditions and boundary conditions for this case were extracted from the ground and flight experimental data for the 1.0gram/s flow rate test section and are listed in Table 8. The fluid domain is initialized with 100% vapor to a uniform temperature and pressure with zero velocity. The inlet mass flow rate (shown in Fig. 9) and inlet temperature were specified according to the test data evolutions. Several inlet void fractions were considered for the *Mixture Cooling* section since the test data shows significant oscillation in the measurement. These were held constant for the first 47 seconds for 1-g and 45 seconds for low-g until pure liquid was injected for the remainder of the simulation. The outlet face is specified as a pressure outlet and set to zero gauge pressure. No-slip boundary conditions are applied to all fluid domain walls and all solid walls are adiabatic. This case was run using only the VOF model for terrestrial and low-gravity conditions.

Table 8.   Initial and boundary conditions, Mixture Cooling + Chilldown 1-g/low-g

Variable	Mixture Cooling + Chilldown 1-g	Mixture Cooling + Chilldown low-g
g, m/s^2	9.81	0.001
$\dot{m}_{inlet}$, gram/s	0.53 [0-27s linear ramp], 1.0 [27-77s]	0.49 [0-20s linear ramp], 1.0 [20-63s]
T_{inlet}, K	97 (mixture), 87 (liquid)	99 (mixture), 84 (liquid)
$T_{initial}$, K	211.7	210.6
T_{sat}, K	93.987	93.987
P_{outlet}, MPaA	0.5	0.5
$P_{initial}$, MPaA	0.5	0.5
$\alpha_{v,inlet}$	1 [0-47s] : 0 [47-77s] 0.95 [0-47s] : 0 [47-77s] 0.9 [0-47s] : 0 [47-77s] 0.8 [0-47s] : 0 [47-77s]	1 [0-45s] : 0 [45-63s] 0.8 [0-45s] : 0 [45-63s]
$\alpha_{v,initial}$	1	1
$V_{initial} <i,j,k>$, m/s	<0,0,0>	<0,0,0>
$t_{sim,start}$, s	113	113
$t_{sim,end}$, s	190	176

D. Material Properties

The vapor was modeled as a compressible ideal gas. Temperature-dependent properties were used for both phases. All the thermophysical and thermodynamic properties of the fluids were taken from NIST REFPROP Version 9.1 [24]. For the low-g simulations, a zero degree contact angle was used for surface tension modeling. Temperature-dependent material properties for the solid polycarbonate were provided by JAXA.

IV.   Results and Discussion

A. Chilldown 1-g

The experimental temperature data at the sensor locations TA1-1, TA1-2, and TA1-3 are compared to the CFD results in Fig. 10, Fig. 11, and Fig. 12, respectively. Note that all three plots are presented on the same linear scale. For TA1-1 and TA1-2, both CFD predictions lag the experimental values early in the simulation. Around 12 seconds into the simulation, there is a sharp drop in temperature and the chilldown curve slope becomes similar to the experimental data. The EMP results predict a larger temperature drop than VOF indicating a more efficient boiling

heat transfer process. The simulation results lag the experimental values for TA1-1 and TA1-2 because the probes in the CFD models do not quench until the liquid arrives at their axial location. Since the selected window for simulation is in the middle of the experiment, the experimental sensors have already begun to cool down from the vapor-dominant mixture flow that precedes the time at which 100% liquid enters the chamber. The experimental data for TA1-3 shows a small drop in temperature over the simulated window. This response is captured by EMP while VOF fails to predict any cooling of the downstream probe. At the time in the experiment the simulation is started (t_{exp} = 160s), the liquid is unable to reach the dead end so TA1-3 remains relatively constant. This indicates that the flow rate is not high enough to overcome gravity and completely wet the dead end of the chamber.

A sequence of liquid volume fraction scalar plots are shown in Fig. 13, displaying the evolution of the two-phase flow through the slits and providing a comparison between the VOF (left) and EMP (right) models. The VOF prediction shows liquid never reaches the dead end whereas EMP predicts liquid arrival but only for a brief duration. As the liquid-vapor interface approaches the slits, liquid filament structures project through the slits and hit the dead end of the downstream room temporarily quenching the wall. Once the liquid-vapor interface moves through the slits, the liquid filament structures lose momentum, fall back to the interface, and no longer reach the dead end. This highlights the strength of EMP to capture continuous-dispersed phase distributions.

Still frames from the ground experiment are given in Fig. 14 showing the progression of the two-phase flow. The times associated with the frames correspond to the experiment. Droplets are seen hitting the dead end as the bulk liquid rapidly boils. Once the bulk liquid flows through the slits, the droplets no longer reach the dead end as predicted with the EMP model. The EMP model is capable of predicting dispersed phases; however, to capture many droplets entrained in a flow, a Lagrangian solver must be used. In the experiment, it is possible that prior to a 0% quality condition at the inlet (before t_{exp} = 160s), the vapor-dominant mixture flow contains many liquid droplets entrained in the vapor and is seen in the video still frames. During this time, all three probes are cooled by convection of the mixture. Once the bulk liquid moves through the slits, no wetting of the dead end occurs.

Another difference between the two multiphase models is that EMP predicts convective cooling at the temperature sensor locations prior to liquid arrival whereas the VOF temperatures are constant until liquid arrival. This is likely due to the EMP model predicting a large amount of vapor generation, and the stronger capability to define liquid-vapor phase interactions in the closure models. The dispersed vapor phase rises into the vapor region above the liquid-vapor interface due to buoyancy. The vapor is near saturation temperature and diffuses into the warm vapor region above the liquid. The velocity of the vapor carries it downstream and convectively cools the probes prior the liquid arrival. In addition, the warm liquid is displaced through the outlet and is replaced by boil-off. The VOF model does not predict enough vapor generation to have a substantial cooling effect in the vapor region above the interface, and it lacks sophisticated liquid-vapor phase interactions.

Note that vapor generation was not tracked and the solution is a result of using defaults in the boiling models. These conclusions are made by observations from the volume fraction and temperature scalar field evolutions displayed in Fig. 15 and Fig. 16 for VOF and EMP, respectively. Liquid volume fraction is shown on the left and temperature on the right. The VOF results show that the temperature field propagates downstream at the same rate as the liquid volume fraction indicating the arrival of the liquid is providing the wall cooling. The EMP temperature field propagates much faster downstream than the liquid-vapor interface providing convective cooling prior to liquid arrival from the boil-off. Note that the EMP model was built for subcooled boiling and to be "pushed" towards saturated boiling whereas a chilldown process starts in the film boiling regime and transitions into the nucleate regime. Similarly, the VOF model does not accurately model the film boiling regime and only applies a heat flux once the wall superheat is within the transition boiling regime.
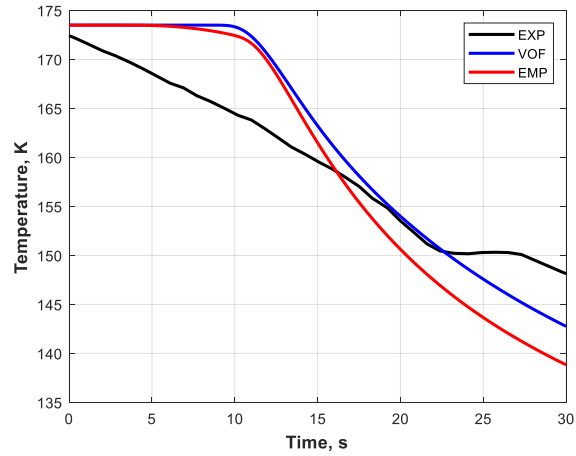
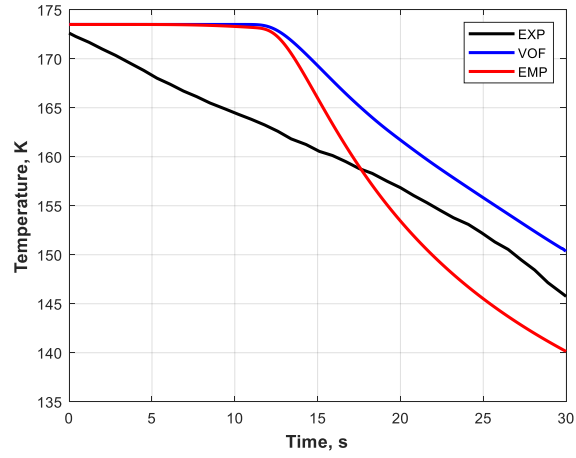**Fig. 10   TA1-1 temperature profiles for Chilldown 1-g**

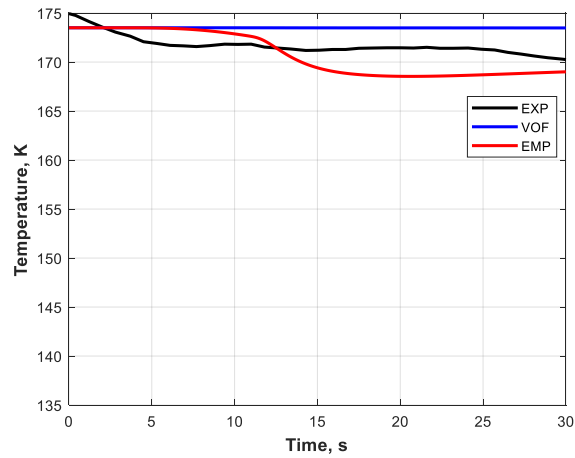**Fig. 11   TA1-2 temperature profiles for Chilldown 1-g**

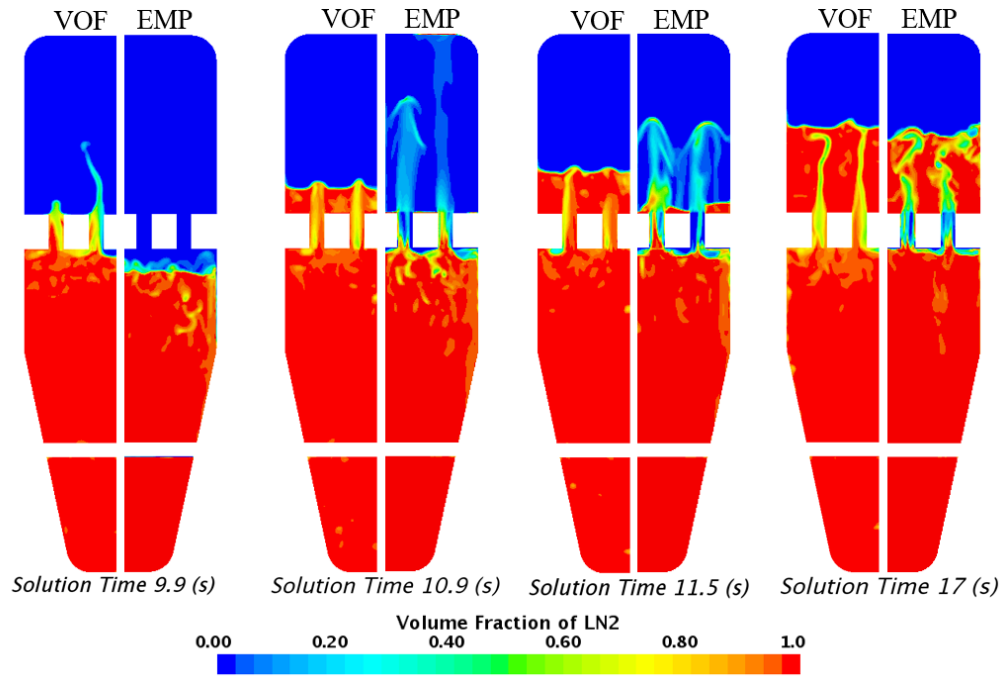**Fig. 12   TA1-3 temperature profiles for Chilldown 1-g**

Fig. 13   Comparison of liquid volume fraction evolution between VOF (left) and EMP (right)
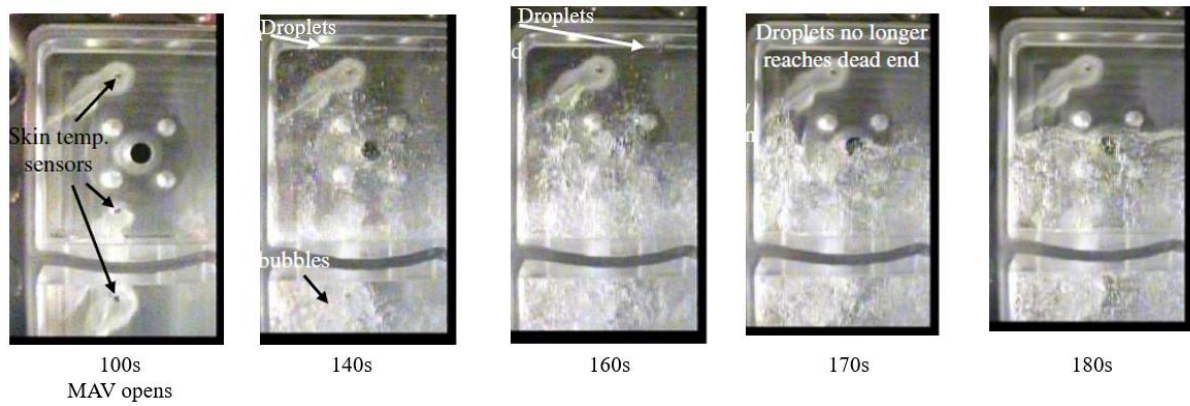

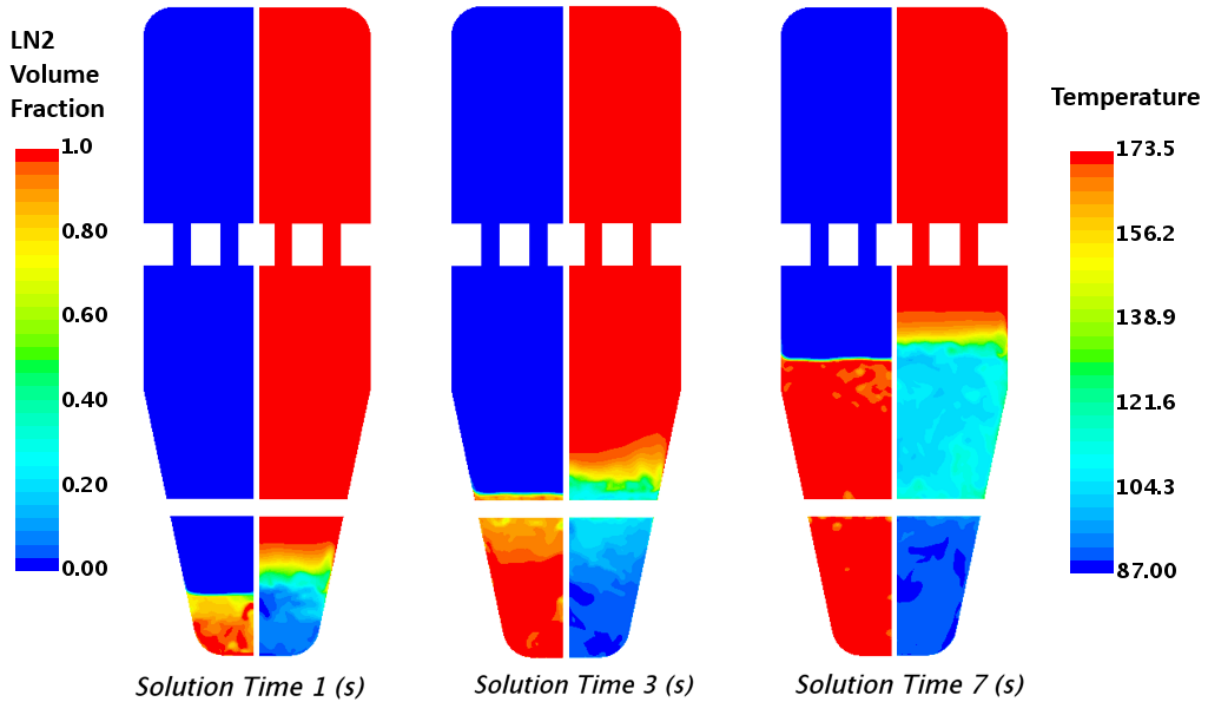**Fig. 14   Still frames from ground experiment showing two-phase flow [7]**

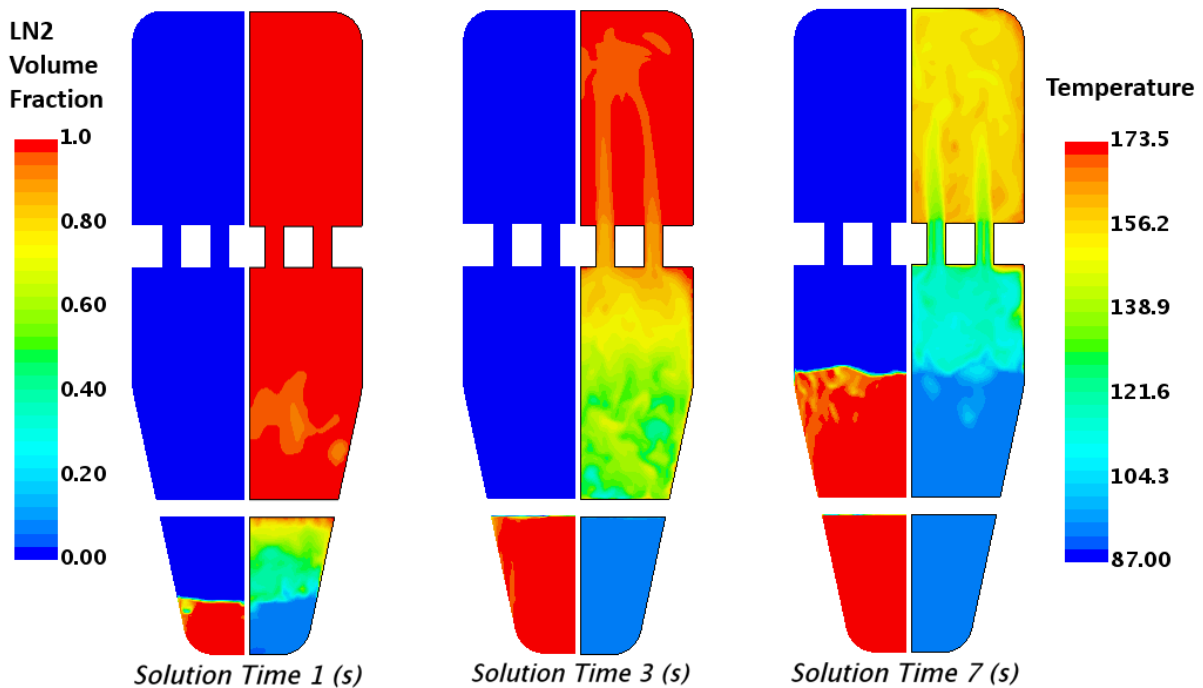**Fig. 15   Evolution of liquid volume fraction (left) and temperature (right) using VOF**

Fig. 16   Evolution of liquid volume fraction (left) and temperature (right) using EMP

B. Liquid-Vapor Mixture Cooling + Chilldown 1-g

Several inlet mixture ratios were considered for the *Mixture Cooling + Chilldown 1-g* case presented in Table 8. The mixed volume fraction inlet condition was used until 47 seconds and then 100% liquid was specified for the remainder of the simulation. The experimental temperature data at the sensor locations TA1-1, TA1-2, and TA1-3 are

18

compared to the CFD results in Fig. 17, Fig. 18, and Fig. 19, respectively. The 90% and 95% void fraction simulations compare well to the test data while the 100% and 80% void fraction cases over- and under-predict the chilldown curve, respectively. This observation agrees well with the test data shown in Fig. 4 where the void fraction oscillates near 0.9-0.95 before dropping to zero. For the two upstream probes TA1-1 and TA1-2, the larger the liquid percentage the faster the cooling rate. The 0% and 5% liquid cases level off just after the inlet condition switches from mixed to pure liquid and cooling is delayed until the liquid arrives similar to the *Chilldown 1-g* case presented in the previous section. The larger liquid percentage cases do not demonstrate this behavior because a substantial amount of liquid accumulates in the upstream room during the mixture cooling. Once pure liquid is injected, it takes less time for the liquid to reach the probes. For TA1-3, the 0%, 5%, and 10% all are comparable, however, the 20% case demonstrates significantly less cooling. Since the inlet flow rate is the same for each combination, the cases with lower liquid percentages will have higher mixture velocities and lower densities. The higher velocities contribute to a more effective convective cooling process. In addition, the 20% liquid mixture flow has a larger density and slower velocity so gravity has a stronger effect. This mixture flow loses momentum through the slits and does not reach the dead end in the downstream room.

This study demonstrates that for much of the experiment, the probes were convectively cooled by a liquid-vapor mixture until the feed line into the test chamber was sufficiently chilled to saturation temperature and provided a void fraction of zero. Deviations in the CFD results from the experimental data can be attributed to assumptions in the mass flow rate profile and boiling models.
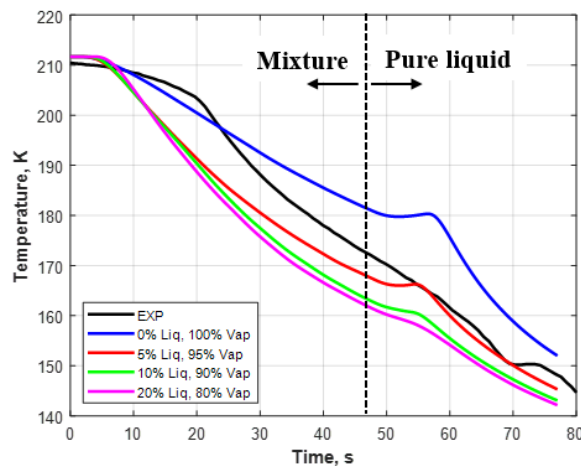

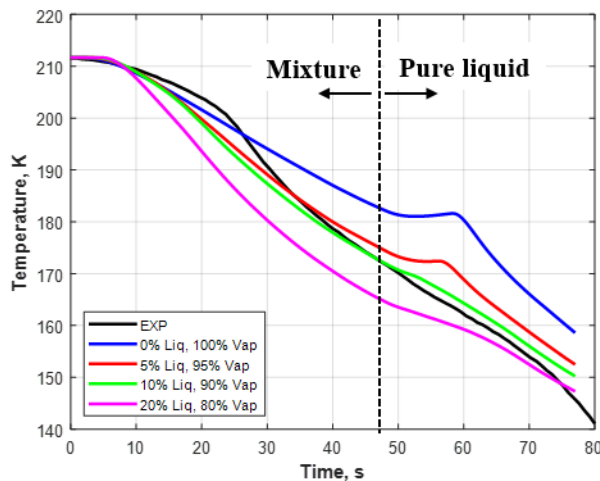**Fig. 17   TA1-1 temperature profiles for Mixture Cooling + Chilldown 1-g**

Fig. 18   TA1-2 temperature profiles for Mixture Cooling + Chilldown 1-g
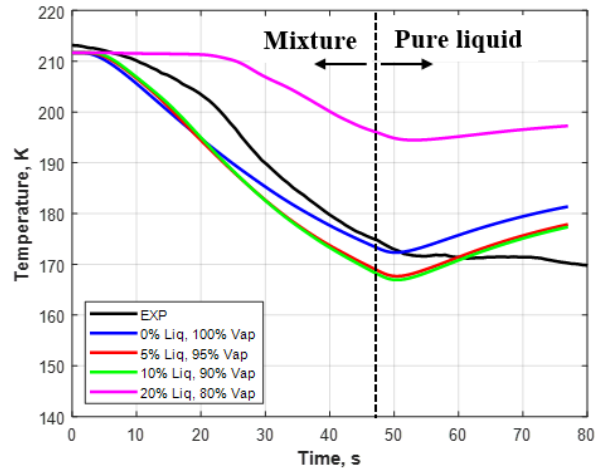
19

Fig. 19   TA1-3 temperature profiles for Mixture Cooling + Chilldown 1-g

C. Liquid-Vapor Mixture Cooling + Chilldown Low-g

Two inlet mixture ratios were considered for the *Mixture Cooling + Chilldown Low-g* case presented in Table 8. The mixed volume fraction inlet condition was used until 45 seconds and then 100% liquid was specified for the remainder of the simulation. The experimental temperature data at the sensor locations TA1-1, TA1-2, and TA1-3 are compared to the CFD results in Fig. 20, Fig. 21, and Fig. 22, respectively. Similar to the 1-g case, the mixture ratio that closely resembles the void fraction data shown in Fig. 4 compares well to the experimental temperature profiles.

The main difference between the ground and flight experiment is that all three probes chill down in the flight experiment whereas the TA1-3 probe does not completely chill down in 1-g. As stated earlier, once the liquid-vapor interface moves through the slits, gravity pulls on the liquid prohibiting it from wetting the dead end wall in the downstream room. In a low-gravity environment, the surface wettability is enhanced and allows the liquid to spread along the walls chilling down all three probes. The liquid volume fraction evolution predicted by the VOF solver is displayed in Fig. 23, highlighting the flow behavior under low-g conditions.

Still frames from the flight experiment are given in Fig. 24 showing the progression of the two-phase flow in the experiment. The times associated with the frames correspond to the experiment. The CFD simulation predicts a large steady bubble just upstream of the slits as seen in the experiment. Also, small bubbles in the downstream room are captured correctly. The ability of the CFD solver to capture the flow driven by surface tension is promising for future low-g flow studies.
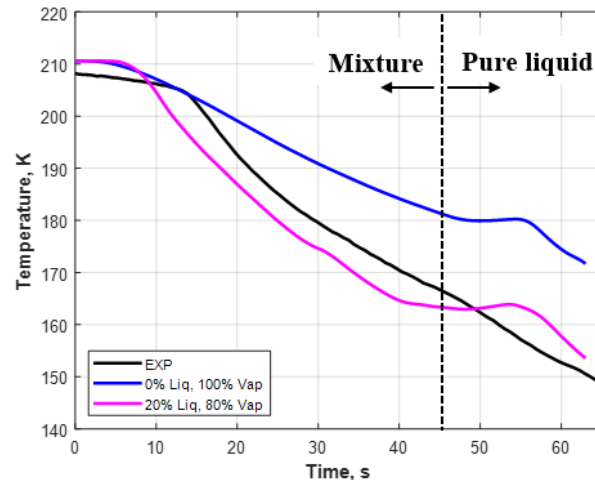

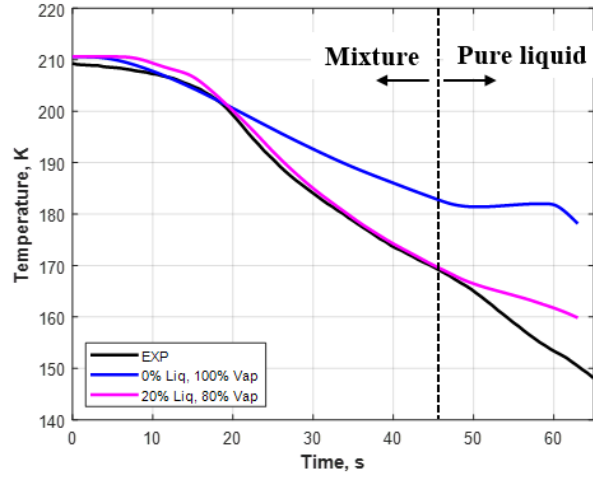**Fig. 20   TA1-1 temperature profiles for Mixture Cooling + Chilldown Low-g**

20

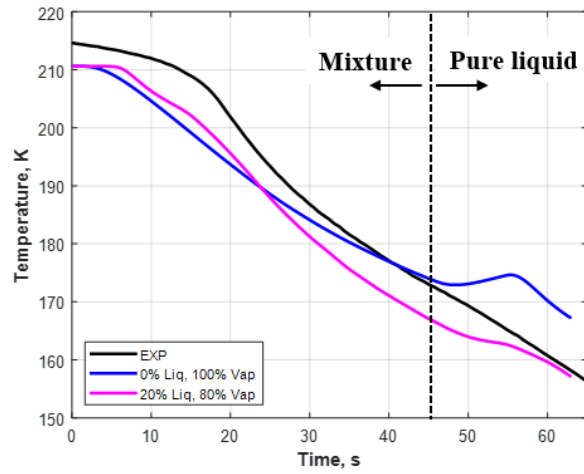**Fig. 21   TA1-2 temperature profiles for Mixture Cooling + Chilldown Low-g**

Fig. 22   TA1-3 temperature profiles for Mixture Cooling + Chilldown Low-g
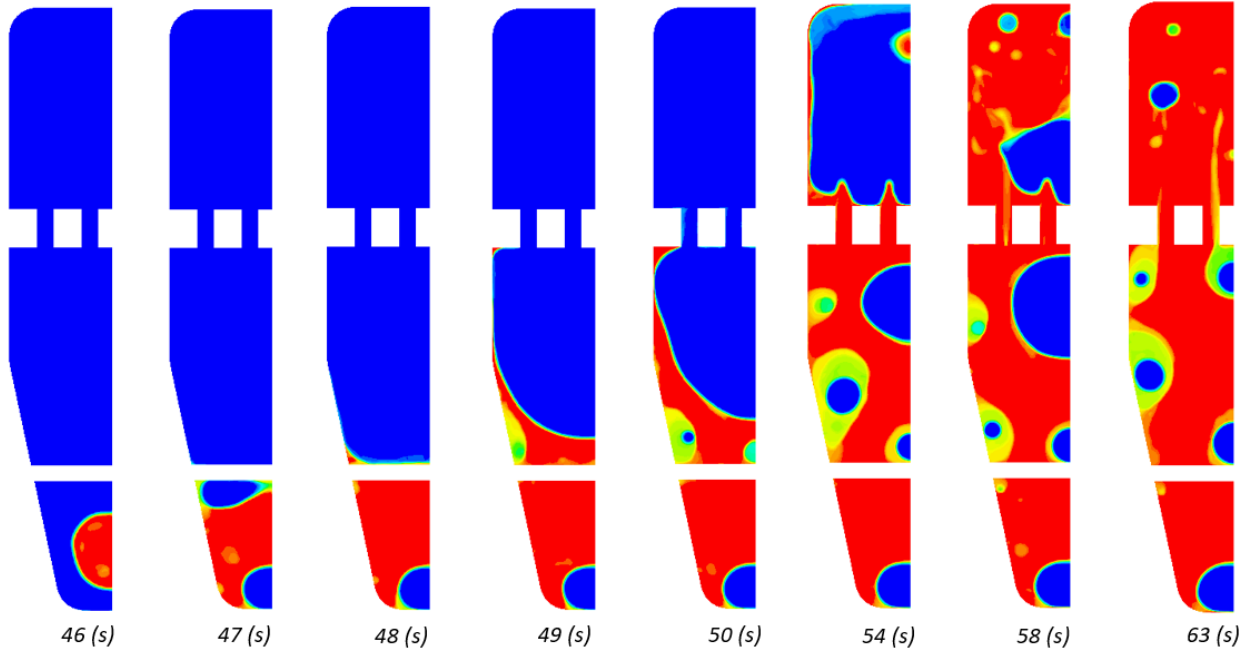
Fig. 23   Liquid volume fraction evolution for Mixture Cooling + Chilldown Low-g
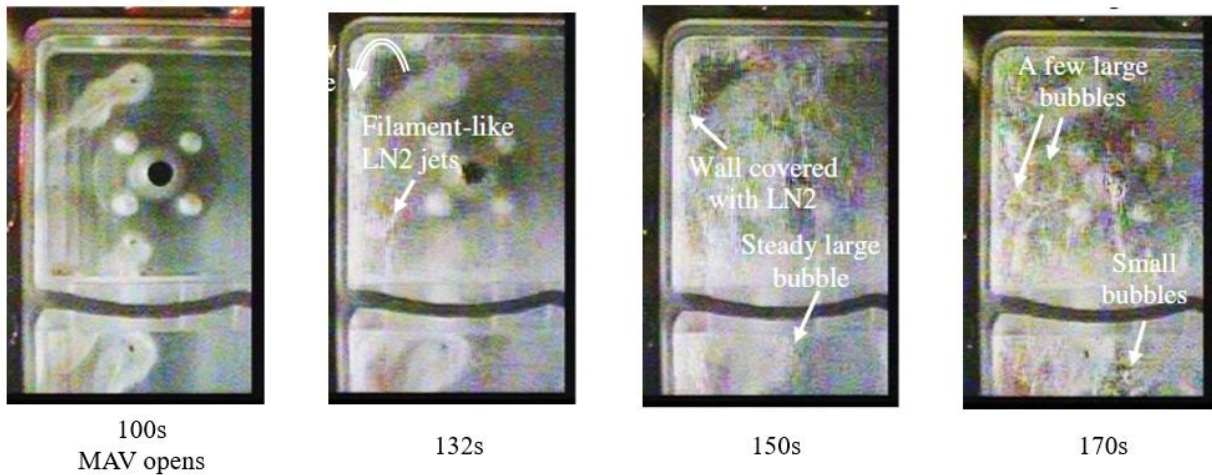

Fig. 24   Still frames from flight experiment showing two-phase flow [7]

V.   Conclusion

Ground and suborbital flight experiments were conducted by JAXA to investigate cryogenic chilldown of a complex channel. Three experimental temperature sensors were used to evaluate the chilldown process and to compare with CFD results for validation. Commercial CFD code STAR-CCM+ was used to model the problem with both the Volume of Fluid method and Eulerian Multiphase Segregated Flow model. Each method has its own boiling model which was evaluated and compared.

For the *Chilldown 1-g* case, the EMP and VOF CFD results compared reasonably with the experiment by predicting a similar slope of the chill-down curve and overall temperature drop over the selected window of the experiment. The EMP model predicted liquid to hit the dead end of the downstream room highlighting its ability to capture continuous-dispersed phase distributions and agreed with the still frames from the experiment. In addition, the

22

EMP model predicted a larger amount of vapor generation that resulted in noticeable convective cooling of the probes prior to liquid arrival. The VOF model failed to predict liquid to hit the dead end and did not predict any convective cooling prior to liquid arrival.

The VOF model was used to solve the *Mixture Cooling + Chill-down 1-g/Low-g* simulations. The CFD results do a reasonable job at predicting the chilldown of the experimental temperature sensors for both cases. Varying the inlet condition showed that the chamber was convectively cooled by the mixture until the inlet reached a 0% quality condition. For the low-g case, the flow was driven by surface tension effects, and the enhanced wettability in a low gravity environment was demonstrated. Flow features predicted by the CFD model were seen in the experiment giving confidence in the prediction.

Overall, the CFD modeling provided insight into the challenges associated with validating cryogenic chilldown. Future work should focus validation studies on simpler problems such as a highly-controlled vertical pipe cryogenic chilldown experiments that exist in the literature. Studies with well-defined boundary conditions (inlet quality) should be pursued, and experiments with flow visualization are of interest to validate the phase distribution in the CFD models.

Acknowledgements

References

[1] Schuster, J.R., Howell, D.J., Lucas Jr., S.L., Haberbusch, M.S., Gaby, J.D., Van Dresar, N.T., and Wadel, M.F., "Cold Flow Testing of Revised Engine Chilldown Methods for the Atlas Centaur," *32nd AIAA-96-3014*, 32nd Joint Propulsion Conference, Lake Buena Vista, FL, July 1 – 3,1996.

[2] Schuster, J.R., Bassett, C.E., Christensen, E.H., Honkonen, S.C., Merino, F., Munko, D.S., Pietrzyk, J.R., and Wollen, M.A., "Centaur-Based Liquid Hydrogen Fluid Management Flight Experiments," *AIAA-91-3539*, AIAA/NASA/OAI Conference on Advanced SEI Technologies, Cleveland, OH, September 4 – 6, 1997.

[3] Tanner, C., Young, J., Thompson, R., and Wilhite, A., "On-Orbit Propellant Resupply Options for Mars Exploration Architectures," *AIAA-2006-261*, IAC-06-D1.1.01. 2006.

[4] Hartwig, J.W., McQuillen, J.B., and Rame, E. "Pulse Chilldown Tests of a Pressure Fed Liquid Hydrogen Transfer Line" *AIAA-2016-2186, AIAA SciTech Conference* San Diego, CA, January 4 – 8, 2016.

[5] Merte, H., "Incipient and Steady Boiling of liquid Nitrogen and Hydrogen Under reduced Gravity," NASA Technical Report No. 7, Report 07461-51-T, The University of Michigan, Contract NAS-8-20228, November, 1970.

[6] Darr, S.R., Dong, J., Glikin, N., Hartwig, J.W., Majumdar, A., LeClair, A., and Chung, J.N., "Effect of Gravity on Cryogenic Flow Boiling and Chilldown," Nature Microgravity 2, 16033. 2016.

[7] Kinefuchi, K., Sarae, W., Umemura, Y., Fujita, T., Okita, K., Kobayashi, H., Nonaka, S., Himeno, T., Sato, T., "Investigation of Cryogenic Chilldown in a Complex Channel Under Low Gravity Using a Sounding Rocket," *Journal of Spacecraft and Rockets,* Vol. 56, No. 1, 14 Sept. 2018. doi: 10.2514/1.A34222.

[8] Grayson, G., Lopez, A., Chandler, F. et al., "CFD Modeling of Helium Pressurant Effects on Cryogenic Tank Pressure Rise Rates in Normal Gravity" NASA-TM- 20080015652, July 2007.

[9] Kartuzova, O. and Kassemi, M., "Modeling K-Site LH2 Tank Chilldown and no Vent Fill in Normal Gravity" AIAA-2017-4662, 53rd Joint Propulsion Conference, Salt Lake City, UT, July 10 – 12, 2017.

[10] Kassemi, M. and Kartuzova, O., "Effect of Interfacial Turbulence and Accommodation Coefficient on CFD Predictions of Pressurization and Pressure Control in Cryogenic Storage Tank" Cryogenics 74, 138-153. 2016.

[11] Umemura, Y., Himeno, T., Kinefuchi, K., Saito, Y., Hartwig, J.W., Hauser, D., Y., Sakowski, B., Johnson, W., LeClair, A., and Fukasawa, O. "Numerical Simulation on Liquid Hydrogen Chill-down Process of Vertical Pipeline" 2019 Joint Propulsion Conference August 19 – 21, 2019.

[12] Siemens Simcenter STAR-CCM+, Ver. 14.02.010-R8 (2019.1), Plano, TX, 2019.

[13] Kinefuchi, K., Sarae, W., Aoki, K., Himeno, T., Nonaka, S., and Okita, K., "Upper Stage Propulsion System Development for H-IIA Upgrade," Proceedings of the 4th European Conference for Aerospace Sciences, Saint Petersburg, Russia, 2011.

[14] Zhang, H., Mudawar, I., and Hasan, M., "Flow Boiling CHF in Microgravity," *International Journal of Heat and Mass Transfer* 48, 3107 – 3118. 2005.

[15] Brackbill J. U., Kothe, D. B., Zemach, C., "A continuum method for modeling surface tension," *J. Comp. Phys.* Vol. 100, 1992, pp. 335–354.

[16] Koster, J., Sani, R., *Low Gravity Fluid Dynamics and Transport Phenomena*, Progress in Astronautics and Astronautics, AIAA, c.1990, pp. 53.

[17] Podowski, M.Z. and Podowski, R.M., "Mechanistic Multidimensional Modeling of Forced Convection Boiling Heat Transfer", Science and Technology of Nuclear Installations, Article ID 387020, 10 pages, 2009.

[18] Lemmert, M. and Chawla, J.M., "Influence of flow velocity on surface boiling heat transfer coefficient", Heat Transfer in Boiling, E. Hahne and U. Grigull, Eds., Academic Press and Hemisphere, New York, NY, USA, 1977.

[19] Tolubinsky V.I. and Kostanchuk D.M., "Vapour bubbles growth rate and heat transfer intensity at subcooled water boiling", Heat Transfer 1970, Preprints of papers presented at the 4th International Heat Transfer Conference, Paris, 5, Paper No. B-2.8.

[20] Bartolomei G.C. and Chanturiya V.M., "Experimental study of true void fraction when boiling subcooled water in vertical tubes", Thermal Engineering, 14, 1967, pp 123 – 128.

[21] Cole R., "A photographic study of pool boiling in the region of the critical heat flux", AIChE J., 6, 1960, pp. 533 – 542.

[22] Del Valle M.V.H. and Kenning D.B.R., "Subcooled flow boiling at high heat flux", Int. J. Heat Mass Transfer, 28, 1985, pp. 1907 – 1920.

[23] Kurul, N. and Podowski, M.Z., "Multidimensional effects in sub-cooled boiling", Proceedings of the Ninth Heat Transfer Conference, Jerusalem, 1990.

[24] NIST REFPROP, Ver. 9.1, Boulder, CO, 2013.

[25] Umemura, Y., Himeno, T., Kawanami, O., Sarae, W., Kinefuchi, K., Kobayashi, H., Fukasawa, O., "Liquid Nitrogen Chill-down Process Prediction by Direct Interface Tracking Approach," *53rd AIAA/SAE/ASEE Joint Propulsion Conference*, July 2017. doi: 10.2514/6.2017-4761